Kaon scattering from C and Ca at 800 MeV/c

D. Marlow, P. D. Barnes, N. J. Colella,*
S. A. Dytman,† R. A. Eisenstein, R. Grace
F. Takeutchi,‡ and W. R. Wharton
Carnegie-Mellon University, Pittsburgh, Pennsylvania 15213

S. Bart, D. Hancock, R. Hackenberg, E. Hungerford,
W. Mayes, L. Pinsky, and T. Williams§
University of Houston, Houston, Texas 77004

R. Chrien, H. Palevsky, and R. Sutter
Brookhaven National Laboratory, Upton, New York 11973
(Received 14 December 1981)

Results from $K^{\pm}$ elastic and inelastic scattering from ^{12}C and ^{40}Ca are reported. The data were all taken at an incident momentum of 800 MeV/c over an angular range from 2° to 38°. The elastic data are compared to first-order optical model calculations in coordinate and momentum space; good qualitative agreement is obtained. The inelastic data (from ^{12}C only) are compared to distorted-wave Born approximation calculations, and good agreement is found if "realistic" inelastic transition densities are used. Although a first-order optical potential description does not describe the data fully, there are strong indications of the increased penetrability of K^+ over K^- in this energy range.

[NUCLEAR REACTIONS ^{12}C($K^{\pm},K^{\pm}$)^{12}C, ^{40}Ca($K^{\pm},K^{\pm}$)^{40}Ca, E =442 MeV (800 MeV/c), measured $\sigma(\theta)$ for elastic and inelastic scattering, compared to optical model and DWBA calculations, deduced optical potential parameters; θ=2°–38°, $\Delta\theta$=1°.]

I. INTRODUCTION

One of the major tasks of medium energy physics is to understand better how to construct the many-body meson-nucleus interaction from the more basic meson-nucleon amplitudes. This requires not only knowledge of the basic two body input, but also a prescription for its use in a many-body calculation, the end result of which will be a prediction to be compared with data. In this way we hope to construct a good many-body theory of strong interactions which will provide guidance not only in the nuclear case, but also in other problems as well.

The simplest of these processes that one can address are elastic and inelastic scattering of mesons from nuclei. For pions, such a program is now well underway. An extensive body of data now exists and many calculations, stressing different aspects of the problem, have been made. Several reviews of this subject have been written, and the reader is referred to Refs. 1–3 for more details. For both pions and kaons the calculations have been of two kinds: (1) rather simple optical potential formulations[4–9] which in varying degrees of approximation represent the multiple scattering series; and (2) "doorway" theory results,[10–15] which focus primarily on the dynamics of bound πN or KN systems in the nuclear medium. Both kinds of calculations have indicated the need for careful treatment of the two body t matrix, true absorption, off-shell behavior, nucleon binding, and Fermi motion, as well as other effects associated with the nuclear medium.

The reasons for interest in the kaon-nucleus problem are mostly due to the differences between the basic KN and πN amplitudes. As will be discussed, these differences are fundamental and arise in large measure because of the nonzero strangeness of kaons. In Sec. II we describe the features of the KN interaction and the naive expectations for K-nucleus scattering. In Sec. III the apparatus and experiment

are described; the data are presented and compared to theory in Sec. IV. Conclusions drawn from the work are given in Sec. V.

II. THEORY

The kaons form four members of the octet of pseudoscalar mesons, shown in Fig. 1. The $K(\bar{K})$ systems form an isodoublet of strangeness $+1(-1)$, while the pions and the eta are the nonstrange members of the group. Thus, while the $K^{\pm}$ are antiparticles, they are not members of the same isodoublet and so their strong interactions cannot be linked by isospin invariance. An examination of the total $K^{\pm}$-N cross sections shows this clearly (see pp. 40–41 of Ref. 16). Below 1 GeV/c, the $K^-(S=-1)$ cross section shows the existence of many narrow resonances, both in the $I=0$ (Λ) and $I=1$ (Σ) channels. The approximate cross section at 800 MeV/c is $\sim$42 mb/sr for the $I=0$ (K^--N) channel. Figure 2 shows the total K^-p and K^-n cross sections calculated using the amplitudes of Ref. 17. The positions of prominent K^-N resonances are listed in Table I.

On the other hand, the K^+ ($S=1$) data are smoothly varying, apparently without resonance structure in this momentum range. Figure 3 shows a more detailed view of the K^+p and K^+n total cross section over the momentum range 0–1200 MeV/c as described by Martin. As the energy increases, each partial wave enters gradually and monotonically. Of interest is the fact that at 800 MeV/c the total cross section is $\sim$13 mb/sr for K^+, and that partial waves up to at least $l=2$ are required to describe the data. The lack of resonance structure is due to the absence of any hadrons with strangeness $+1$. In a quark picture (see Fig. 4) a K^+N resonance requires formation of five-quark objects, which have never been observed.

We are thus dealing with a situation quite different from the one presently existing for proton or pion scattering. In the medium energy range, the proton-nucleon amplitudes are nonresonant but fairly large (35 mb/sr at 800 MeV) and contain important spin-dependent pieces. The pion-nucleon cross section above 100 MeV pion kinetic energy is dominated by the (3,3) resonance which is quite broad ($\sim$100 MeV) and very large ($\sim$200 mb/sr at 275 MeV/c in π^+-p). For both of these systems, there are no open channels other than charge exchange below the π production threshold. In contrast, the K^--N system has many narrow resonances ($\Gamma\sim 15-40$ MeV) and there are open channels down to the K^--N threshold. The cross sections are roughly comparable to those for NN scattering. Therefore, we expect that the K^--nucleus cross section will reflect these features: The interaction will be strong and the amplitude complicated. On the other hand, the K^+-*nucleus* cross sections should be fairly weak and the amplitudes reasonably simple. In fact, we expect the K^+-nucleus interaction to be the weakest of any strongly interacting probe, and the resulting mean free path to be large. We note that there is no true absorption of the K^+ to complicate things, in distinction to the case for low energy π-nucleus scattering, where the mean free path is also large.

In order to construct a K-nucleus theory, a prescription must be used for extrapolation from the two-body (KN) to the A-body system. Owing to the paucity of experimental data, comparatively little effort has been made toward the building of a sophisticated theory. Most calculations[4–9] of which we are aware use first order multiple scattering theory (Rayleigh-Lax or Glauber) in which the factorization approximation has been invoked. With such a form, the optical potential becomes

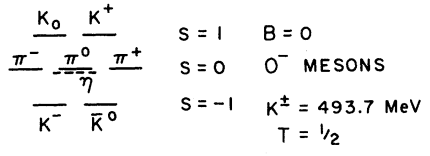

FIG. 1. The pseudoscalar meson octet.

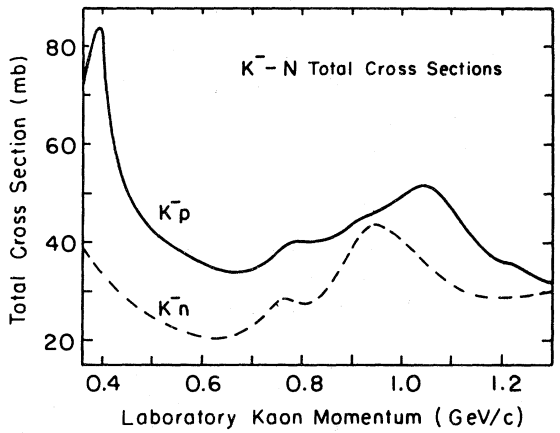

FIG. 2. The K^-p and K^-n total cross sections calculated using the amplitudes of Ref. 17. The positions of several of the more important resonances are given in Table I.

TABLE I. Prominent resonances in the K^-N system. (See Ref. 16.)

Y^* isobar	L	J^P	Width (MeV)	K^-_{lab} (MeV/c)	% $\bar{K}N$
$\Lambda(1405)$	0	$\frac{1}{2}^-$	40±10	below threshold	
$\Lambda(1520)$	2	$\frac{1}{2}^-$	15±2	392	46%
$\Lambda(1670)$	0	$\frac{1}{2}^-$	40±20	735	15–35
$\Lambda(1690)$	2	$\frac{1}{2}^-$	55±25	777	20–30
$\Lambda(1815)$	3	$\frac{1}{2}^+$	85±15	1044	60
$\Sigma(1670)$	2	$\frac{1}{2}^-$	50±15	735	10–25
$\Sigma(1750)$	0	$\frac{1}{2}^-$	75±25	905	10–40
$\Sigma(1765)$	2	$\frac{1}{2}^-$	130±20	937	41

proportional to the product of the two body amplitude $t(k,k')$ and the nuclear density $\rho(q)$. In the calculations shown below, the kaon amplitudes were taken from Martin[19] in the case of K^+ or from Alston-Garnjost *et al.* (Ref. 17) in the case of K^-. The nuclear densities were taken from electron scattering data[21] (see also Table VI).

In our calculations, we have made use of both coordinate[22] and momentum space[23] formulations. The latter treatment provides a convenient means of studying potentially important effects such as off-shell behavior, the angle transformation, and Fermi motion. The Kisslinger potential,[1]

$$2EV(r)=Ak^2b_0\rho(r)+Ab_1\vec{\nabla}\cdot\rho\vec{\nabla}$$

was used in the coordinate space calculations, with appropriate kaon values for the parameters b_0 and b_1. A more detailed description of these matters can be found in Refs. 1–9 and in Sec. IV.

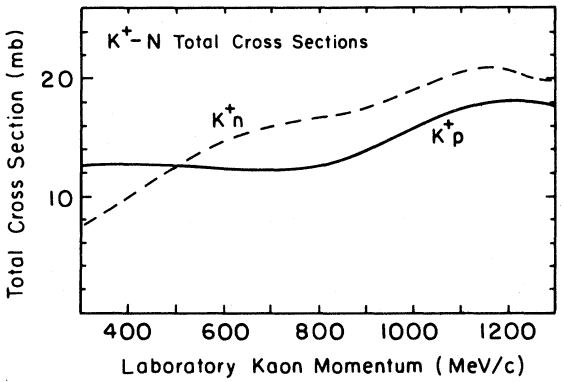

FIG. 3. The total K^+p and K^+n cross sections calculated using the amplitudes of Ref. 19.

III. APPARATUS

A. The low energy separated beam

The experiment was performed using kaons from the low energy separated beam (LESB I) at the Brookhaven alternating gradient synchrotron (AGS). The kaons were produced by interactions of the 28.5 GeV/c primary proton beam with the nuclei of the platinum production target. The AGS typically delivered 4×10^{12} protons to the production target in each one second burst. Successive bursts were spaced by 2.2 s.

The LESB I beam line has been described in detail elsewhere, hence only a brief description will be given here. A layout of the beam line is shown in Fig. 5. Kaons leaving the production target at an angle of 10.5° with respect to the primary proton

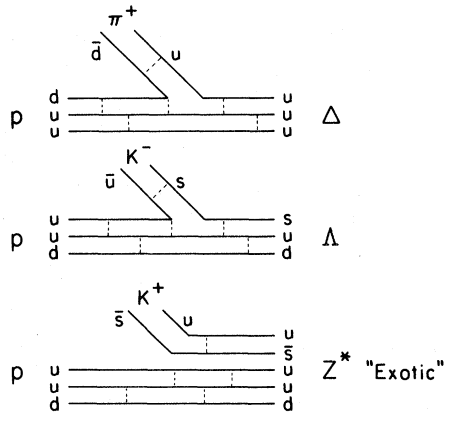

FIG. 4. Diagrams showing Δ and Λ formation in π^+p and K^-p interactions. A resonance in K^+p scattering requires formation of a 5 quark object.

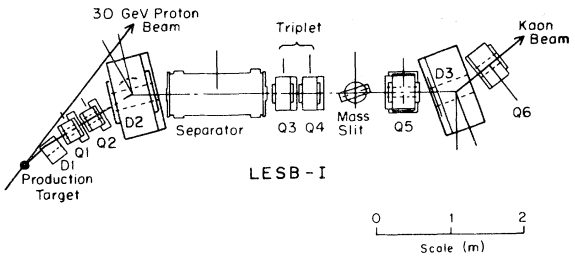

FIG. 5. Schematic diagram of the LESB I beam line.

beam enter the first dipole, $D1$, which sweeps particles of the wrong momentum from the beam. Once through $D1$, the particles pass through $Q1$ and $Q2$ where they are focused to be parallel to the beam axis in the horizontal and vertical planes for transit through the vertical separator.

The separator operates at a potential difference of 550 kV across a 10 cm gap, and selects particles of the desired mass through the combined action of crossed electric and magnetic fields. After traversing the full 210 cm length of the separator, the particles pass through two more quadrupoles, $Q3$ and $Q4$, where they are focused vertically on the mass slit. $D2$, which is located further upstream, provides dispersion at the mass slit.

At the mass slit, the particles deflected by the separator are absorbed, or at least severely degraded, and thereby removed from the beam. Furthermore, the horizontal momentum dispersion provided by $D2$ allows one to select a narrow range of momenta through the use of a second set of slits that define a horizontal aperture. Kaons of the desired momentum, however, pass through the slits to the final three elements of the LESB I beam line. These elements, designated $Q5$, $D3$, and $Q6$, provide a final bend and produce the desired focus of the beam delivered to the hypernuclear spectrometer system.

With a primary proton intensity of 4×10^{12} protons per burst, LESB I delivers about 150000 K^- and 510000 K^+ per burst at 800 MeV/c. These rates were observed at the exit of LESB I and thus do not include losses incurred in the spectrometer used for momentum analysis of the beam. The larger K^+ intensity reflects the larger production cross section for this particle relative to the K^-. Although the electrostatic separator served to reject a large fraction ($>99\%$) of the particles of the wrong mass, a considerable background of unwanted particles, mainly pions, remained in the beam. For a K^- beam the ratio of K^- to unwanted background particles was about 1:12, while the corresponding ratio for K^+ was 1:13.

B. The trigger

Most of the particle identification was done using a trigger consisting of time-of-flight (TOF) information and a kaon differential Cerenkov counter. This resulted in rejection of almost all of the pion background. This was crucial, as otherwise the trigger rate would have been unmanageably high.

The time-of-flight counters form an essential part of the experimental trigger. The positions of the three counters are shown in Fig. 6. $S1$ defines the beam as it leaves LESB I to enter the spectrometer and provides the start signal for the first (beam) leg of the TOF system. ST, located 11 cm upstream of the experimental target, provides the stop signal for this leg and defines the beam at the target.

The observed timing resolution for minimum ionizing particles traveling between $S1$ and ST is 1.4 ns FWHM, resulting in a clean separation between π's and K's. However, a slight background of pions from accidental coincidences remains.

A similar arrangement is employed in the second (scattering) leg of the spectrometer. In this leg, the start signal is provided by ST and the stop signal is provided by $S2$. Here the observed resolution is 800 ps FWHM (see Fig. 7). The slightly worse timing resolution in the beam leg is caused by the high singles rates at the exit of LESB I. Under these conditions, space charge effects limited the maximum voltage that could be applied to $S1$ to a value lower than what would have been optimal for the best time resolution.

Two Cerenkov detectors were used to improve the particle identification in the spectrometer legs. The first, located just upstream of $S1$ at the exit of LESB I, was of the critical angle type and sensitive only to kaons. The Cerenkov angles for 800 MeV/c pions and kaons traversing a Lucite radiator ($n=1.49$) are such that the pion light is trapped inside the plastic by total internal reflection while the

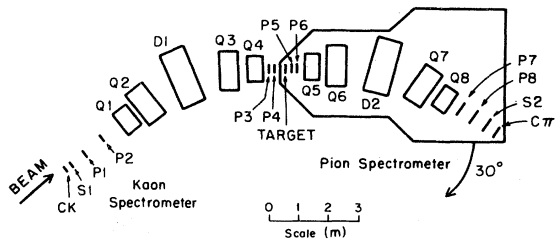

FIG. 6. Schematic diagram of the Moby Dick spectrometer system. The scintillator ST is located at the target position.

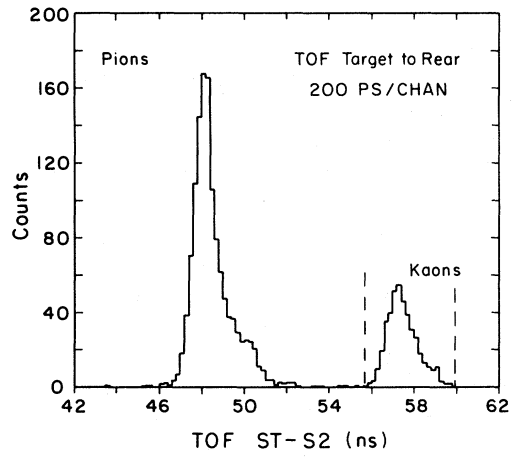

FIG. 7. Time-of-flight spectrum showing the excellent separation between π and K projectiles at 800 MeV/c. Vertical lines indicate the timing cut used on line.

kaon light escapes to strike one of six phototubes positioned in a ring outside the plastic. This counter provided a rejection factor for pions of approximately 10 000:1.

The second Cerenkov detector was positioned past $S2$ at the end of the spectrometer. The larger angular divergence of the beam at this point dictated the use of a threshold type Cerenkov counter. Having an active area of 33×50 cm, and using 10 cm of LN_2 as a radiator, this counter was 97% efficient for 800 MeV pions.

Trigger signals used to initiate the reading of data by the on line computer were generated via the following scheme. Particle types were identified in the individual legs of the spectrometer by separate measurements of their times of flight and the proper Cerenkov counter signals. Thus, fast coincidence signals corresponding to kaons and pions in each spectrometer were formed. Next, these "subtrigger" signals from the individual legs were combined to generate complete triggers. For example, the main data trigger, i.e., the (K,K) trigger, was formed by requiring a coincidence between the signals indicating a kaon in both legs of the system. Other triggers, such as the (π,π) and (K,π) triggers, were formed in a similar fashion.

The timing windows were chosen to be sufficiently generous to pass all but a negligibly small fraction of the desired particles. A typical on line cut is indicated by the vertical lines in Fig. 7. The small fraction of pions accepted at the trigger level were easily eliminated in the off line event analysis.

C. The wire planes

The energy resolution requirements of the experiment created the need for accurate position information. Therefore, three digital readout multiwire proportional chamber (MWPC) modules were placed in each leg of the spectrometer. Each of the six modules consisted of three separate measurement planes. In principle, two orthogonal planes would have been sufficient to determine completely the position of a particle; however, the addition of a third plane lent redundancy that assured high detection efficiency. This was especially important for the three chambers that were situated directly in the kaon beam. In these chambers, the high particle fluxes resulted in a large amount of primary ionization which in turn led to the tendency for space charge buildup in the wire planes, lowering the gas gain of the chambers. By requiring only two of the three planes of a module to fire, good detection efficiencies ($>99\%$ for all modules) were maintained.

The high rates also called for the use of digital readout techniques. Each wire was instrumented with a separate amplifier, discriminator, and delay circuit. The trigger pulse, generated as described above, was used to form a coincidence with the delayed pulses of the hit wires. The outputs of the coincidence circuits were then fed to latch circuits used to store the results for readout by the on-line computer.

D. The hypernuclear spectrometer (Moby Dick)

The momentum analysis of the incoming and scattered kaons was performed by the hypernuclear spectrometer, nicknamed "Moby Dick." As indicated by its name, the spectrometer was originally designed for use in experiments to study the formation of hypernuclei via the (K^-,π^-) strangeness exchange reaction. However, the spectrometer also lent itself well to the (K,K) reaction which is the topic of this paper. No significant modification of the system was needed.

Moby Dick has been described by its designers (Ref. 24), and the reader interested in a more detailed description than the one given here is referred to that document.

The spectrometer consists of two legs as indicated in Fig. 6. The first leg rests upstream of the experimental target and provides a momentum analysis of

the beam kaons on an event-by-event basis. The second leg rests on a movable platform and provides a similar analysis on kaons scattering from the experimental target. The currents in the magnets of the second spectrometer are set to produce a tune having a larger solid angle acceptance, in view of the fact that the scattered beam will occupy a much larger angular range than does the beam emerging from LESB I. Knowledge of the momenta of the beam and scattered kaons allows one to deduce the kaon energy loss and consequently the excitation of the recoil nucleus.

Position measurements from the three wire chambers in each leg are combined with magnetic matrix elements, calculated to second order using the program TRANSPORT,[25] to deduce the momenta of charged particles passing through the magnets. Once the momenta are known the trajectories can be fully reconstructed in each leg. Thus all the information necessary to calculate the kinematic variables of interest, i.e., the excitation energy of the recoil nucleus and the scattering angle, are available.

Unfortunately, the additional path length introduced by the beam spectrometer arm of Moby Dick causes a large reduction in kaon beam intensity. For the most part, this loss of beam can be attributed to kaon decays. The decay length of an 800 MeV/c kaon is very nearly 6 m, thus one expects that at least 75% of the beam will decay along the 8 m flight path of the beam spectrometer. In addition, there are transmission losses that also reduce the beam intensity. The measured rates per pulse (4×10^{12} incident protons) at the experimental target were 18 500 and 6200 for K^+ and K^-, respectively. The corresponding rates for π^+ and π^- were 234×10^3 and 240×10^3. Comparing this to the rates at the entrance to LESB I and correcting for the decay losses, one deduces that the transmission for kaons is 47% and that the transmission for pions is 13%. Presumably, the poor transmission of pions occurs because of the effect of the electrostatic separator on the pion beam phase space obtained when the separator is tuned for a kaon mass separation.

E. Event analysis

The selection of good events and rejection of background starts with the requirement of a good track in each of the spectrometers. At a minimum, we required that there be at least one hit (i.e., 2 of 3 planes) in each of three chambers in both legs of the spectrometer. Moreover, the rather high charged particle fluxes in the first spectrometer resulted in a significant (30%) fraction of events wherein at least one of the three chambers had more than one hit. This fraction is in fact much larger than the fraction one would expect from a straightforward calculation of the accidentals rate. Evidently, the raw data contained a number of false triggers generated by chance coincidences that stimulated (K,K) events. For this reason we required that there be no more than one hit in each of the first three chambers; i.e., the chambers in the beam leg of the spectrometer. The effect of this cut on the excitation spectrum is shown in Fig. 8.

Assuming that the vertical trajectories of the particles are independent of their momenta (true to first order), one sees that the Y measurements made at the two chambers nearest the target constitute redundant measurements. The vertical positions at these chambers can be calculated from the measured positions and angles at chambers $P2$ and $P5$. Thus by subtracting the measured values from the calculated values one obtains an error quantity whose value is zero for an ideal event. In practice, measurement errors in the wire planes and higher order corrections to the matrix elements result in a distribution with a finite width, even for good tracks. Nonetheless, by placing cuts on these redundant variables, one rejects a number of events that correspond either to in-flight kaon decays or scattering from the magnet pole tips.

The distribution of this quantity, referred to as Y-Y', is shown for each spectrometer in Fig. 9. The cuts applied to tracks in the first (beam) spectrome-

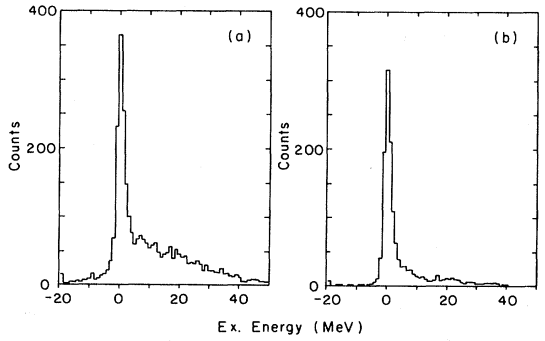

FIG. 8. Excitation spectra (a) before and (b) after the application of the multiplicity cut. The cut requires that there be one and only one hit in each of the three beam chambers.

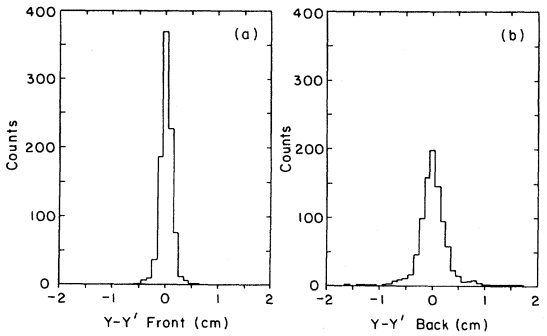

FIG. 9. Histograms of the Y-Y' variables in (a) front and (b) rear spectrometers. Both plots were generated from the same sample of clean events. The width of the rear distribution is larger because of the larger phase space occupied by the particles entering the rear spectrometer.

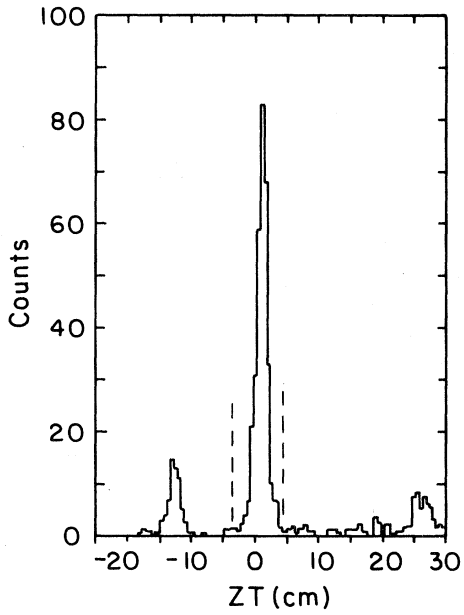

FIG. 10. Histogram of the Z vertex reconstruction for a sample of elastic scattering. Zero of the abcissa is at the target position, while the small peak to the left is caused by kaons scattering from a small plastic scintillator, ST, located upstream of the target.

ter are rather stringent whereas the cuts applied to the tracks in the rear spectrometer are considerably more generous. In the former case, erroneously rejected events are not too worrisome since the same cut is applied to a sample of beam events resulting in the cancellation of systematic errors. In the latter case, however, erroneously rejected events are a potential source of systematic error; therefore only conservative cuts are applied in anticipation of more powerful cuts to be applied later in the analysis.

By and large, the remaining sources of background can be rejected by requiring that the event vertex lies within the known target volume. The beam trajectories can be projected to the target position in both the horizontal and the vertical. Events whose projected positions miss the target can then be rejected. Like the Y-Y' cut, these cuts introduce no systematic error since they are applied both to the scattering event candidates and to a sample of beam events.

The Z position, i.e., the position along the beam axis of the reconstructed vertex, provides a powerful tool for the rejection of background events. Clearly, the Z coordinate of an actual nuclear scattering event must lie near the target (defined to be $Z=0$), whereas most background events are more or less evenly distributed along the Z axis.

Examples of such background sources include kaon decays and scattering from the air in the target region. Moreover, a large number of spurious "events" are generated either by random coincidences between unrelated tracks in the two spectrometers or by scattering from the magnet pole tips. The apparent Z positions of these events also tend to be evenly distributed along the Z axis. In addition, the raw data sample includes a number of events where the kaons have scattered from ST, the TOF scintillator resting 11 cm upstream of the target. These events are easily rejected by the Z vertex requirement. A typical Z vertex spectrum is shown in Fig. 10.

The scattering angle is calculated taking into account the direction of not only the scattered particle, but of the incident beam particle as well. Using the latter information is essential since by failing to do so the resulting angular resolution for the scattering angle would be entirely dominated by the angular divergence of the incident beam (32 mrad FWHM). Fortunately, the position information from the chambers allows an improved angular resolution to be obtained. Multiple scattering in the target, the spatial resolution of the wire chambers, and higher order corrections to the magnetic matrix elements all contribute to the observed resolution.

It is possible to measure the angular resolution directly by using the $K\rightarrow\mu\nu$ decay mode of the kaon. Since there are only two bodies in the final state, the decay angle of the outgoing muon is given by the following expression:

$$\theta_{\text{lab}}=\arccos\left[\frac{\epsilon_K\epsilon_\mu-m_K\epsilon_\mu^*}{p_K p_\mu}\right]. \quad (1)$$

Here ϵ_K and ϵ_μ are the total laboratory energies of the kaon and muon, p_K and p_μ are their laboratory momenta, and ϵ_μ^* is the energy of the muon in the kaon rest frame. The above expression allows one to make use of the good momentum resolution of the spectrometer to make an accurate (2 mrad FWHM) measure of the decay angle. The result is considerably better than a measurement made using only geometric information from the wire chambers.

Therefore, by comparing the measured angle to the angle calculated using the procedure outlined above, the effective angular resolution of the spectrometer can be determined. This was done and the results are shown in Fig. 11 plotted in the form of a histogram of the quantity

$$\Delta\theta=\theta_{\text{calc}}-\theta_{\text{measured}}$$

for a sample of $K\to\mu\nu$ decay events. Subtracting a small correction to account for errors in the momenta used in Eq. (1), one deduces an angular resolution of 0.66° FWHM. The sample of events histogrammed in Fig. 11 was obtained with the experimental target removed. To determine the actual angular resolution obtained during the data taking, one must quadratically add the contribution of multiple scattering in the target (0.76° FWHM for the ^{12}C target and 0.88° for the ^{40}Ca target) to the number obtained from the width of the peak in Fig. 11. The resulting angular resolutions are 1.01° and 1.10° for carbon and calcium, respectively.

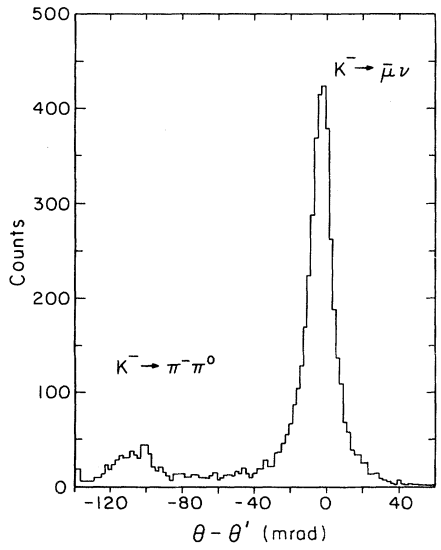

FIG. 11. The quality of the scattering angle reconstruction is shown. Both the $K^-\to\mu^-\nu$ and $K^-\to\pi^-\pi^0$ channels were observed. (See text.)

The value of the excitation energy is mainly determined by the measured energy difference between the incident and scattered kaons, but a small correction for the recoil energy of the massive nuclear target is needed. The magnitude of this correction is, of course, determined by the scattering angle and the mass of the target nucleus.

Typical ^{12}C excitation energy spectra are shown in Fig. 12. The spectrum of Fig. 12(a) was accumulated with the spectrometer set to 12.5° and is dominated by the elastic scattering peak; only a small number of events is seen in the region of the inelastic states (positive excitation energy). The spectrum in Fig. 12(b) was accumulated with the spectrometer set to 20.5°. The excitation of inelastic states is quite evident. In particular, the 2^+ state at 4.4 MeV is clearly resolved from the elastic peak. The third peak, near 10 MeV, is the well known 3^- state at 9.6 MeV excitation. However, the experimental energy resolution is not good enough to eliminate contaminants from other states nearby. These include the 0_2^+ (7.66 MeV), 0_3^+ (10.1 MeV), and 1^- (10.84 MeV).

Even though the procedures described in the preceding paragraphs eliminate most of the background events, a small residual contamination remains in the final event sample. A rough estimate of the magnitude of the background can be obtained by observing the number of events falling

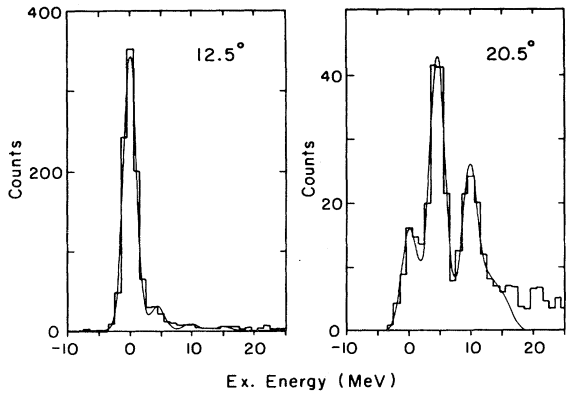

FIG. 12. Excitation spectra and best-fit curves for the reaction ^{12}C(K^-,K^-). The fitting procedure is described in the text. Data shown are for selected one-degree angle bins. The spectrometer angle settings are shown in the figure.

far to the left ($E_x < -5$ MeV) of the elastic peak. Events falling in this region are unphysical, implying a net energy gain on the part of the scattered kaon. Their number, although small, is too large to be accounted for by the tail of the elastic peak; probably they belong to an additional flat background. Scattering from the magnetic pole tips is a possible source of this background.

Peak areas of the elastic and the low-lying inelastic states were extracted using standard least squares minimization techniques. The program MINUIT (Ref. 26) was used to search for the minimum of the function

$$\chi^2=\sum_i \left[\frac{Y_i(x_i)-F(x_i,P_1,P_2,\ldots P_n)}{\sigma_i}\right]^2,$$

where Y_i is the number of observed counts in the bin centered at the energy x_i, σ_i is the corresponding error, and $F(x_i,P_1,P_2,\ldots P_n)$ is a function used to describe the data. The variables P_j are the parameters to be varied.

The excitation spectrum was parametrized as a sum of Gaussian curves plus a flat background, i.e.,

$$F(x_i,P_1,P_2,\ldots P_n)=\sum_j N_j \exp\left[\frac{1}{2}\left[\frac{x_i-x_j}{\sigma_j}\right]^2\right]+B,$$

where each Gaussian peak is written as a function of three parameters. The energy spacings of the low lying states studied in this experiment are well known. Furthermore, the peak widths observed in this experiment were determined by the energy resolution of our apparatus, and are therefore the same for all states in a particular spectrum.

For these reasons, only a single parameter, corresponding to the peak area, was used for each peak included in the fits. Three additional parameters were used to vary the common peak width, the overall offset of the experimental energy spectrum, and the height of the flat background.

Typical spectra for the $^{12}C(K^{\pm},K^{\pm})$ and the $^{40}Ca(K^{\pm},K^{\pm})$ reactions are shown along with the corresponding best fit curves in Figs. 12 and 13. In the ^{12}C case, excitation of the 0^+ (7.60 MeV) state was assumed to be negligible. Also, the energy resolution of our apparatus was not good enough to identify positively the low-lying excited states in our ^{40}Ca spectra. Included in the observed excitation are the $J_p=3^-$ state at 3.73 MeV, the $J_p=2^+$ state at 3.90 MeV, or a mixture of both. These states were included in the fits in order to allow extraction of the elastic peak area but are not tabulated in the results published here.

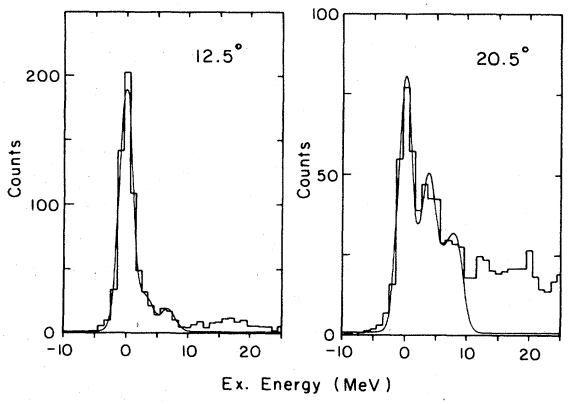

FIG. 13. Excitation spectra and best-fit curves for the reaction $^{40}Ca(K^+,K^+)$. See Fig. 12.

F. Monte Carlo calculation of the solid angle

By using the wire chamber information, it was possible to obtain an angular resolution considerably smaller (see Sec. III E) than the ± 6 degree range accepted by the spectrometer. This justified dividing the data into one degree angle bins. Therefore, in addition to knowing the total solid angle acceptance of the spectrometer, it was also necessary to know the angular shape of the acceptance. (In order to check consistency, the data were taken in angular steps smaller than the spectrometer angular acceptance.)

The last unknown quantity needed to calculate the cross section is the effective solid angle $\Omega(\theta_i,\theta_j)$ for each 1° wide angle bin at each scattering angle θ_i and each spectrometer angle θ_j. By keeping θ_i fixed and varying θ_j in steps of 1° or 2° about θ_i, the variation of $\Omega(\theta_i,\theta_j)$ with θ_j can be empirically mapped out. Unfortunately the accuracy of this procedure was sometimes limited by the statistical error in the yield. Furthermore, $\Omega(\theta_i,\theta_j)$ was also dependent upon run-to-run variations in the beam distributions. Variations in the spatial location and angular spread of the beam had a small but non-negligible effect on the solid angle $\Omega(\theta_i,\theta_j)$ because of their obvious effect on the scattering geometry.

To improve the evaluation of $\Omega(\theta_i,\theta_j)$ a Monte Carlo program was used based on the second order TRANSPORT formalism. The trajectories of simulated events, drawn from an isotropic angular distribution, were traced from their origins in the experi-

mental target through the rear spectrometer. Among other things, the solid angle of the rear spectrometer is determined by the physical dimensions of the apertures defined by the pole faces of the magnets. Thus, the positions of the simulated trajectories were compared with known physical dimensions of the magnet apertures and rejected if they were found to lie outside of the apertures. In practice, the pertinent dimensions were those of a vacuum pipe running through the magnets.

By keeping track of the number of events generated in each scattering angle bin, and comparing it to the number of events surviving the entire length of the spectrometer, the effective solid angle could easily be calculated using

$$\Omega(\theta_i,\theta_j)=\frac{N_{\text{good}}}{N_{\text{tries}}}\Omega_0(\theta_i)\ ,$$

where N_{tries} is the number of events generated in the bin θ_i for a particular spectrometer angle θ_j. N_{good} is the number of those events surviving, and $\Omega_0(\theta_i)$ is the maximum possible solid angle for the angle bin in question given by

$$\Omega_0(\theta_i)=2\pi[\Delta\cos\theta_i]\ ,$$

where $\Omega_0(\theta_i)$ is a function of the angle corresponding to the bin center.

The beam profile events, collected simultaneously with normal event data, were used as input to the Monte Carlo calculation. The incoming beam momentum and two-body scattering kinematics were used to calculate the momenta of the simulated outgoing particles. By using actual beam data, it was possible to take into account not only run-to-run variations in the beam phase space, but also correlations between distributions of the variables used to describe the incident beam. Rewardingly, the Monte Carlo calculation of $\Omega(\theta_i,\theta_j)$ agreed with the empirical derivation of $\Omega(\theta_i,\theta_j)$ to within statistical errors for all sets of angles with $(\theta_i-\theta_j)<5°$.

After completing the Monte Carlo study of $\Omega(\theta_i,\theta_j)$ all data in each one degree scattering angle bin, θ_i, was summed over the spectrometer angles θ_j, with appropriate weight given for the beam flux, target thickness, and solid angle $\Omega(\theta_i,\theta_j)$. In this way differential cross sections could be calculated. The results are given in Tables II–IV for all states studied in this experiment.

As a check on the Monte Carlo calculation and the various other aspects of the overall normalization procedure, we have compared our measurements of kaon scattering from a CH_2 target to previously measured kaon-proton cross sections. The results of the comparison are shown in Fig. 14(a). The agreement between our measurements and those of other authors is satisfactory and consistent with our estimated overall normalization uncertainty of $\pm 17\%$ (systematic).

Another check of the overall normalization can be obtained from the $K\rightarrow\mu\nu$ decay measurements. Since the Jacobian for this reaction can be obtained from simple kinematics, a comparison (as a function of angle) can be made of the experimentally measured value to the predicted value. Since the experimental value depends on the Monte Carlo calculation of the solid angle, the comparison is an excellent check of the normalization. Results of this study are shown in Fig. 14(b) where the theoretical and experimental Jacobians are plotted as a function of angle. Neither the data nor the line have renormalized to enhance the agreement.

IV. INTERPRETATION

We turn now to an examination of the data. Figure 15 shows all of the elastic $K^{\pm}$ data for ^{12}C and ^{40}Ca. The data extend roughly over the angular range of 2 to 38°, which was limited by physical constraints of the spectrometer and also by counting rate. The data for both nuclei fall rather sharply with angle and display minima which are characteristic of the nuclear sizes involved. However, they are not sharply diffractive because the basic KN amplitudes are not resonance dominated or particularly absorptive. If one is so inclined, one might conclude that the K^- minima are sharper than those for K^+, but that the K^+ data fall more steeply than the K^-. For both nuclei, the K^+ minima occur at larger angles (typically by about 3°) than for K^-, indicating, if the language of diffraction theory is appropriate, that K^+ sees a smaller nucleus than K^-.

A. Coordinate space calculations

Shown also in Fig. 15 are calculations using the coordinate space optical potential program NPIRK.[22] The predictions shown were generated using a Kisslinger form of the optical potential, viz.,

$$2EV_k(r)=-Ab_0k^2\rho(r)+Ab_1\vec{\nabla}\cdot\rho\vec{\nabla}\ . \qquad (2)$$

While this model is known[1–3] to possess several shortcomings, it represents a convenient starting

TABLE II. Our measured cross sections for K^- scattering from ^{12}C at 800 MeV/c. The overall normalization uncertainty is $\pm 17\%$; the errors listed are statistical only.

		$^{12}C(K^-,K^-)^{12}C$					
		Elastic		2^+ (4.4 MeV)		3^- (9.6 MeV)	
Angle		c.m. cross section		c.m. cross section		c.m. cross section	
lab	c.m.	(mb/sr)	Error	(mb/sr)	Error	(mb/sr)	Error
3.5	3.79	1982.0	572.8				
4.5	4.87	1021.0	195.0				
5.5	5.95	710.10	90.89				
6.5	7.03	613.35	62.56				
7.5	8.11	546.61	48.10				
8.5	9.19	428.69	35.58	4.790	4.330		
9.5	10.28	350.02	28.70	7.927	4.812	1.189	1.427
10.5	11.35	258.97	20.46	6.224	3.112	1.156	1.191
11.5	12.43	192.94	15.24	7.342	2.482	4.149	1.539
12.5	13.51	141.71	10.91	10.595	2.437	3.298	1.346
13.5	14.69	92.269	7.197	11.197	1.937	3.391	1.017
14.5	15.67	62.253	5.105	12.825	1.680	4.346	1.073
15.5	16.75	43.480	3.870	12.810	1.537	3.975	0.950
16.5	17.83	24.121	2.798	10.924	1.289	5.083	1.073
17.5	18.91	15.648	2.128	9.332	1.120	5.446	1.078
18.5	19.99	7.867	1.227	8.844	1.008	4.442	0.911
19.5	21.06	3.760	0.707	7.866	0.889	3.929	0.805
20.5	22.14	2.215	0.490	5.949	0.714	3.596	0.737
21.5	23.21	1.163	0.330	4.594	0.583	3.384	0.670
22.5	24.29	0.951	0.285	3.573	0.518	2.863	0.587
23.5	25.37	1.367	0.339	2.673	0.422	2.014	0.453
24.5	26.44	1.316	0.317	1.743	0.359	1.491	0.346
25.5	27.51	1.391	0.314	1.476	0.314	0.945	0.249
26.5	28.59	1.649	0.351	0.973	0.250	0.852	0.225
27.5	29.66	1.932	0.394	0.363	0.170	0.822	0.217
28.5	30.73	1.515	0.330	0.199	0.139	0.806	0.209
29.5	31.80	1.719	0.370	0.159	0.136	0.373	0.104
30.5	32.87	1.248	0.270	0.127	0.127	0.367	0.149
31.5	33.94	1.227	0.323	0.028	0.030	0.210	0.120
32.5	35.01	0.634	0.244	0.036	0.041		
33.5	36.08	0.212	0.126	0.028	0.025		
34.5	37.14	0.186	0.210	0.317	0.266		
35.5	38.21			0.317	0.234		

point for discussion of the data. In Eq. (2), b_0 and b_1 are complex parameters representing the elementary KN s and p waves. (Higher partial waves, which are present in the t matrix and might be important, are not explicitly included in this model owing to significant ambiguities encountered when generating them in coordinate space.) The density $\rho(r)$ represents the ground state nuclear density.

The parameters b_0 and b_1 were generated (see Table V) according to the prescription in Ref. 5 using the best available phase shift information (Refs. 17–19). For K^+-nuclear scattering, our data showed a clear preference for the parameters generated from the Martin[19] amplitudes over the earlier work of the Bologna-Glasgow-Rome-Trieste (BGRT) collaboration.[20] In both sets of amplitudes, partial waves with $l > 1$ were included and are not small. Therefore, in spite of the difficulty mentioned above, we included these higher waves in an *ad hoc* fashion by adding them to the b_0 term. The result is to change b_0 from $(-0.272, 0.208)$ to $(-0.336, 0.241)$. The b_1 term is unaltered. Since this is a significant change in the potential, it is of interest to treat the higher partial waves correctly.

TABLE III. Our measured cross sections for K^+ scattering from ^{12}C at 800 MeV/c. See Table II.

		$^{12}C(K^+,K^+)^{12}C$					
		Elastic		2^+ (4.4 MeV)		3^- (9.6 MeV)	
Angle		c.m. cross section		Cross section		c.m. cross section	
lab	c.m.	(mb/sr)	Error	(mb/sr)	Error	(mb/sr)	Error
3.5	3.79	971.00	280.62				
4.5	4.87	522.00	99.70				
5.5	5.95	343.32	44.29				
6.5	7.03	299.51	30.25				
7.5	8.11	257.63	20.38				
8.5	9.19	214.80	16.95	1.069	1.069		
9.5	10.28	175.09	13.81	2.937	2.153	0.276	0.256
10.5	11.35	134.36	9.83	3.061	2.103	0.185	0.222
11.5	12.43	104.19	7.65	3.587	1.338	0.625	0.271
12.5	13.51	83.600	5.869	3.390	0.993	1.310	0.356
13.5	14.69	61.899	4.407	3.613	0.954	2.044	0.462
14.5	15.67	50.012	3.456	5.036	0.836	2.230	0.502
15.5	16.75	33.891	2.616	4.978	0.657	2.585	0.545
16.5	17.83	23.335	1.862	6.027	0.711	3.456	0.664
17.5	18.91	16.449	1.336	5.475	0.613	2.887	0.557
18.5	19.99	11.177	0.942	5.483	0.581	3.037	0.568
19.5	21.06	7.380	0.652	4.944	0.514	2.581	0.483
20.5	22.14	4.951	0.525	4.870	0.492	2.890	0.523
21.5	23.21	2.826	0.387	4.494	0.445	2.614	0.471
22.5	24.29	1.744	0.286	3.639	0.368	2.287	0.414
23.5	25.37	1.056	0.216	3.529	0.350	2.337	0.423
24.5	26.44	0.547	0.146	3.057	0.303	1.917	0.345
25.5	27.51	0.302	0.106	2.587	0.264	1.639	0.295
26.5	28.59	0.287	0.096	2.064	0.213	1.534	0.275
27.5	29.66	0.305	0.090	1.613	0.173	1.078	0.201
28.5	30.73	0.215	0.069	1.310	0.143	0.865	0.163
29.5	31.80	0.294	0.076	0.964	0.119	0.626	0.122
30.5	32.87	0.305	0.069	0.552	0.084	0.507	0.104
31.5	33.94	0.291	0.066	0.421	0.073	0.418	0.088
32.5	35.01	0.247	0.058	0.267	0.057	0.270	0.064
33.5	36.08	0.161	0.046	0.237	0.059	0.240	0.060
34.5	37.14	0.222	0.509	0.181	0.056	0.104	0.040
35.5	38.21	0.111	0.041	0.138	0.053	0.074	0.042
36.5	39.27	0.110	0.049				
37.5	40.34	0.147	0.072				
38.5	41.40	0.023	0.026				

This can be done in momentum space and is discussed below. We note that in spite of the change in b_0, its real part remains repulsive in nature.

For the K^- calculations the amplitudes of Alston-Garnjost *et al.*[17] and also of Gopal *et al.*[18] were used, but there was no discernible difference predicting K^--nucleus scattering. In these calculations, all elementary partial waves were lumped together to give only an effective b_0 (see Table V). No separate term in b_1 was included since the s wave is dominant and the p waves were of about the same size as the higher partial waves. The K^--nucleus interaction is seen to be attractive in nature.

The curves shown for each case in Fig. 15 correspond to different choices of the ground state density. In a strict application of the Kisslinger potential the nuclear density $\rho(r)$ should be the density for *point* nucleons because the elementary t matrix already includes the nucleon finite size. However, using the actual matter distribution is an *ad hoc* way of removing the unphysical zero range incorporated in Eq. (2). The solid curves in Fig. 15 are obtained using unmodified electron scattering densities, and the dashed ones correspond to point nu-

TABLE IV. Our measured cross sections for $K^{\pm}$ scattering from ^{40}Ca at 800 MeV/c. See Table II.

		^{40}Ca$(K,K)^{40}$Ca			
		K^+		K^-	
Angle		c.m. cross section		c.m. cross section	
lab	c.m.	(mb/sr)	Error	(mb/sr)	Error
3.5	3.59	9572.30	2766.4	12932.2	3879
4.5	4.61	4333.60	827.75	7030.0	1342
5.5	5.64	2669.94	341.73	4275.7	538.7
6.5	6.66	1908.67	184.42	2847.4	277.7
7.5	7.69	1322.06	104.57	1817.2	145.8
8.5	8.71	860.28	68.31	1142.2	92.26
9.5	9.74	523.62	41.99	623.29	51.42
10.5	10.76	305.76	23.12	295.88	24.02
11.5	11.79	188.67	14.56	136.30	14.31
12.5	12.81	91.16	7.35	50.76	6.95
13.5	13.84	45.95	3.87	35.21	4.75
14.5	14.86	21.47	2.25	32.35	4.82
15.5	15.88	11.88	1.50	36.72	5.69
16.5	16.91	9.98	1.35	35.41	5.70
17.5	17.93	10.69	1.42	37.13	5.94
18.5	18.96	9.42	1.24	28.24	4.66
19.5	19.97	9.77	1.21	22.69	4.04
20.5	21.00	8.70	0.97	12.10	2.65
21.5	22.03	7.36	0.84	8.26	2.01
22.5	23.05	5.09	0.63	4.26	1.59
23.5	24.07	3.54	0.55	2.12	0.987
24.5	25.10	1.83	0.38	1.08	0.76
25.5	26.12	1.26	0.36	3.01	1.61
26.5	27.14	0.76	0.30		
27.5	28.16	0.51	0.22		
28.5	29.18	0.38	0.19		
29.5	30.21	0.26	0.16		
30.5	31.23	0.37	0.22		
31.5	32.25	0.175	0.178		
32.5	33.27	0.063	0.064		

clear densities. (See Table VI.) The K^+ data are better described by the point densities, which have smaller rms radii, while the K^- seem to prefer the unmodified electron scattering densities. This *may* indicate that the K^+ is penetrating more deeply into the nucleus before interacting. However, this conclusion is not firm because of the caveats associated with the Kisslinger model.

With the exception of the K^+-^{12}C data, the coordinate space calculations, which are unadjusted, reproduce the features of the data quite well. In the K^+-^{12}C case, the minimum in the data is about 2° further backward and somewhat shallower than the calculation. At 24° the data are a factor of 2 larger than the calculation.

If the parameters b_0 and b_1 are allowed to vary freely, excellent agreement can be achieved. This was done to describe the entrance channel as accurately as possible for the inelastic scattering calculations described below. These values are included in Table V and were obtained using the finite-size-corrected parameters in Table VI. Best fits of the K^+ data are obtained by eliminating the s-wave absorption and increasing the real s-wave amplitude. The K^- is quite different in that only a weakening of the real s-wave amplitude is required.

B. Momentum space calculations

As indicated above, there are several inaccurate or ambiguous features associated with the available

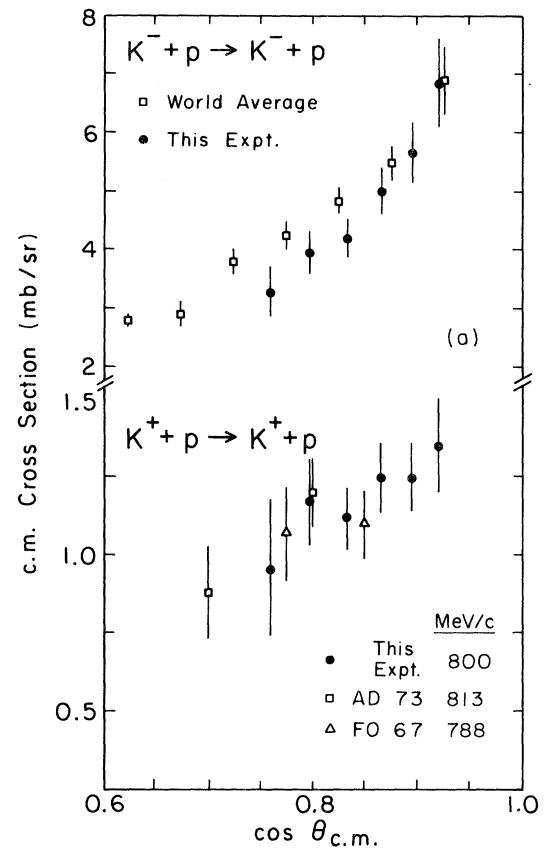

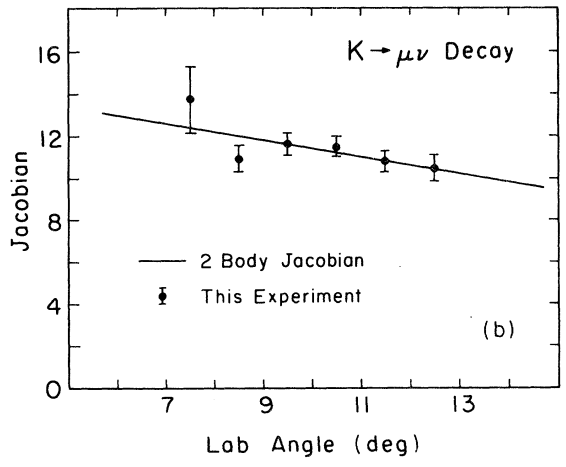

FIG. 14. (a) Center of mass cross sections for K^- and K^+ scattering on hydrogen at 800 MeV/c kaon laboratory momentum. The results of the present experiment are compared with previously published experiments (Ref. 30). Part (b) shows the agreement between a calculation and data from this experiment for the Jacobian of the decay $K^- \rightarrow \mu^- \nu$.

coordinate space optical potentials. On the other hand, momentum space treatments[23] allow precise handling of many of these problems within the context of a first-order factorized optical potential. These include finite KN range, Fermi motion, reasonable off-shell extrapolation, and exact handling of all partial waves in the KN elementary t matrix. It is of interest to see whether these improvements make any substantial difference in the predictions of the first-order theory as handled in coordinate space. A comparison of the data to momentum space calculations using the code KPIT (Ref. 23) is shown in Fig. 16. Also available are total $K^{\pm}$ cross section data,[31] and these agree well with KPIT predictions. (See Table VII.)

The elementary amplitudes were taken from Refs. 17–19; Fermi averaging them according to Ref. 5 made only $\sim 10\%$ differences in the cross section. [An off-shell form factor of the Yukawa type was used, and only very slight ($\sim 10\%$) sensitivity to range was observed, and that at back angles. Values of the Yukawa range parameter of 300 and 800 MeV/c were used in this test. Otherwise, the range used for all calculations was 800 MeV/c.] The nucleon finite size was factored out[23] of the momentum space nuclear density using the Faltung theorem and a nucleon form factor given by

$$\rho_{\text{nucleon}}(q) = (1 + q^2/q_0^2)^{-1} ,$$

with q_0 taken as 4.26 fm^{-1}.

In Fig. 17 we show for K^+-^{12}C elastic scattering both a Born approximation calculation and the full KPIT solution. Except in the minimum region the results are not very different. Thus, the full calculation bears out our naive expectation of a weak interaction, which was inferred from the K^+N amplitude.

After all the above-mentioned effects are taken into account there is little difference to be found between the coordinate and momentum space calculations. In particular, the difficulties with the K^+-^{12}C case, which are the most severe, still persist. It seems as though the first-order factorized optical potential is simply not able to account for the greater penetrability of the K^+, as indicated by the forward angular position of the experimental minima.

Other effects, such as strong coupling of the ground state scattering to that for the 2^+ state, or dispersive corrections, could conceivably influence the first-order calculation. However, Abgrall and

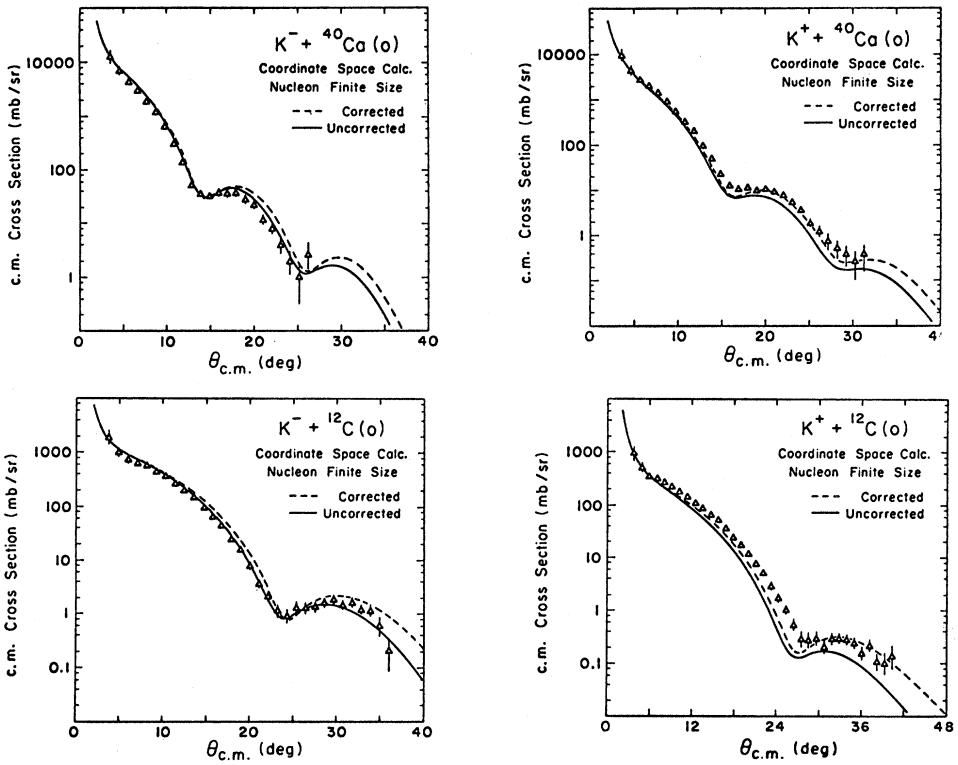

FIG. 15. Comparison of present experimental differential cross sections for $K^{\pm}$ elastic scattering on ^{12}C and ^{40}Ca to curves obtained from the unadjusted Kisslinger model. The dashed ones use electron scattering nuclear densities corrected for finite nucleon size; the solid ones are uncorrected. See text and Tables V and VI.

Labarsouque have shown[8] that dispersive corrections for ^{12}C arising from scattering through the 1^- state (15.11 MeV) are quite small. More work is clearly called for.

TABLE V. Table of the optical model parameters calculated by Rosenthal and Tabakin (Ref. 5). The elementary kaon nucleon amplitudes have been taken from the analyses of Gopal *et al.* (Ref. 18), Martin (Ref. 19), and the BGRT group (Ref. 20). Note that for the K^-, all of the kaon nucleon partial waves have been combined into a single complex parameter, b_0. The best fit parameters for ^{12}C were obtained using the modified harmonic oscillator point nucleon values of Table VI.

	Re(b_0)	Im(b_0)	Re(b_1)	Im(b_1)
K^-				
Gopal	0.61	0.84		
Best fit, ^{12}C	0.32	0.88		
K^+				
Martin	−0.335	0.241	0.084	0.161
BGRT $D(i)$	−0.142	0.209	0.101	0.198
Best fit, ^{12}C	−0.445	0.010	0.035	0.082

C. Inelastic data and calculations

The last results from our experiment to be discussed are the inelastic scattering data obtained for the 2^+ and 3^- states in ^{12}C at 4.4 and 9.6 MeV, respectively. These are shown in Fig. 18 compared to calculations using the coordinate space distorted

TABLE VI. Geometrical parameters of the nuclei studied in the experiment. The ^{12}C density is the modified harmonic oscillator and ^{40}Ca is the three-parameter Fermi (see Ref. 21). The rows labeled "charge density" are unchanged electron scattering values while the "point density" values result after making a correction for nucleon size.

		c	α	
^{12}C	Charge density	1.649	1.247	
	Point density	1.51	2.33	
		c	z	w
^{40}Ca	Charge density	3.766	0.586	−0.164
	Point density	3.671	0.507	−0.065

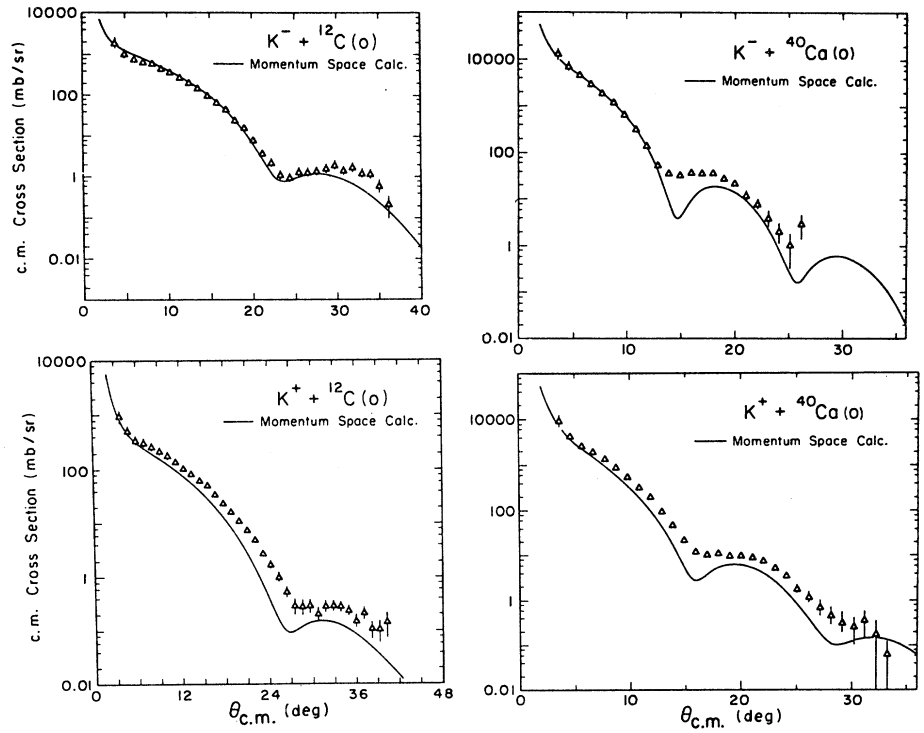

FIG. 16. Comparison of momentum space calculations with the experimental data (see text).

wave program NDWPI.[28] For these calculations, the elastic channel is described using the best-fit optical potential for the elastic data (see Tables V and VI). The inelastic transitions are described using transition densities which are taken from fits to inelastic electron scattering, as presented by Gustaffson and Lambert,[27] or from the particle-hole calculations of Gillet and Vinh Mau,[29] or from the standard derivative form used in the rotational model.[28] These are all of the form

$$\rho_{\rm tr}^{L}(r)=r^{L}(a+br^{2}+cr^{4})e^{-dr^{2}}$$

with the parameters a, b, c, and d depending on the nuclear transition (and model) involved. The three densities so obtained are different from each other, as shown in Fig. 19, and yield different predictions for the angular distributions. Comparing the electron form factor to that for the rotational model shows that the former is larger in the nuclear interior. This fact has a greater influence on the K^+ calculation because the K^+ likely penetrates further into the nucleus than does the K^-. In fact the K^+ obviously requires the electron form factor (see Fig. 18) in order to fit the data (see also Ref. 7). Since

TABLE VII. Comparison of calculated and measured (Ref. 31) $K^{\pm}$-^{12}C total cross sections. All values in mb. Calculations are in momentum space (Ref. 23); see text.

	K^-	K^+
Experiment	338±7	177±1.5
Theory	328	149

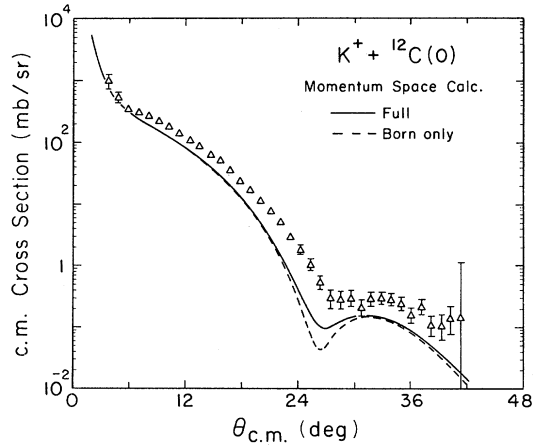

FIG. 17. Momentum space Born approximation calculation (dashed curve) compared to the full calculation. (See text.)

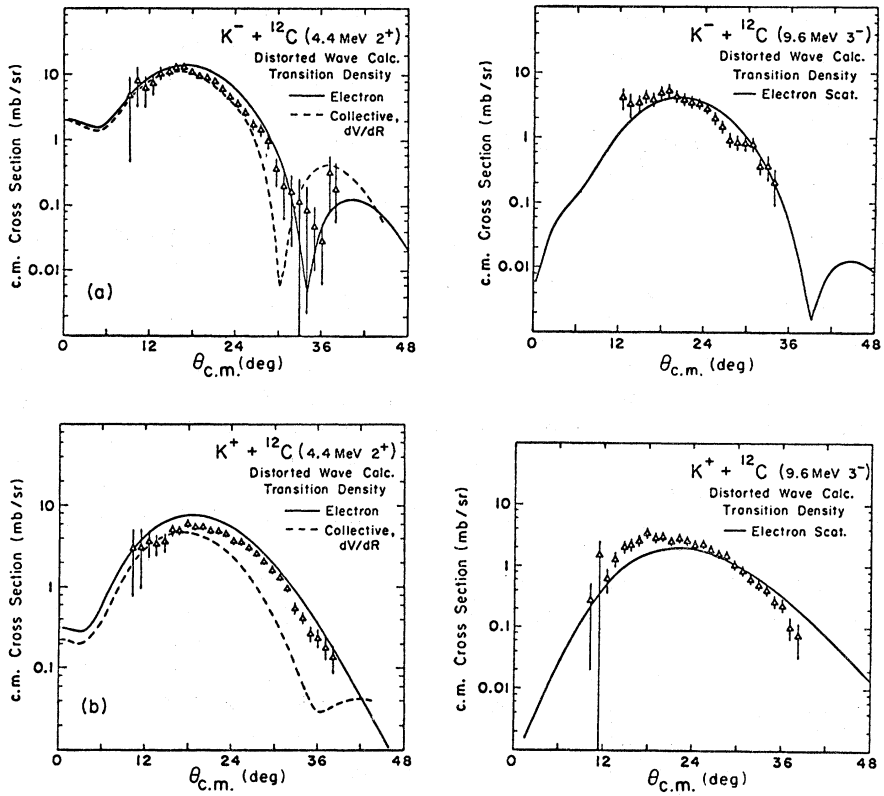

FIG. 18. DWBA calculations for inelastic $K^{\pm}$ scattering to the 2^+ (4.4 MeV) and 3^- (9.6 MeV) states in ^{12}C compared to the data. The solid curves are obtained using the phenomenological electron scattering transition density (Ref. 27); the dashed curves are obtained from the strict rotational model (Ref. 28). See text.

the transition density for a given state is the same for K^- or K^+, the observed experimental differences must be due to the distortions in the elastic channel. These facts lend qualitative support to the statement that the K^+ meson is a strongly interacting but highly penetrating "electronlike" nuclear probe. It is both interesting and satisfying that each of these transitions can be so well described for different projectiles by a common transition density.

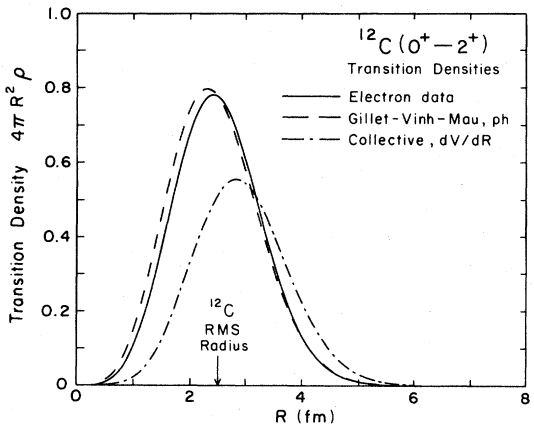

FIG. 19. The three transition densities for the 2^+ state in ^{12}C mentioned in the text. See Refs. 27—29.

V. CONCLUSIONS

$K^{\pm}$ elastic and inelastic scattering data at 800 MeV/c on targets of ^{12}C and ^{40}Ca have been accumulated at the BNL Moby Dick spectrometer facility. The unadjusted first-order kaon scattering calculations presented herein are in reasonable agreement with the elastic data, but are not able to predict simultaneously the K^+ and K^- results with a common nuclear geometry. The K^+-^{12}C case presents the worst discrepancy. Kisslinger model calculations give results quite similar to those from momentum space, which should be more reliable theoretically. This fact indicates the need for better first-order calculations, perhaps using nonfactorized optical potentials and other improvements.

Second-order terms may also be required. This is somewhat surprising in view of the expected weak nature of this interaction. The data are consistent with the idea that the K^+ projectile penetrates more deeply into the nuclear interior than does the K^-, because to fit the former data smaller nuclear sizes must be used in the calculation. The first order theory is apparently unable to account for the deeper penetration of the K^+.

Point nucleon distributions and variable Kisslinger parameters b_0 and b_1 result in excellent fits for the K^+ and K^- data. When these optical potentials are used with electron scattering transition densities in DWBA calculations of the inelastic scattering, excellent agreement is found. This does not occur when the standard rotational form factors are used because these distributions are peaked at larger radii. In the surface region where the K^- interacts the two distributions are not very different, while farther inside where the K^+ interacts they differ considerably.

From the above, we conclude that the claim that the K^+, is the "electron of strong interaction physics" has some validity, although unadjusted first-order theory cannot account for the interaction. It would be quite interesting to explore systematically other nuclei to shed further light on this question. Perhaps we may learn more about nuclear matter distributions away from the nuclear surface in the process.

ACKNOWLEDGMENTS

We would like to thank the staff of the Brookhaven AGS facility and also members of the BNL physics department for their considerable help in mounting and executing the experiment. Morgan May, one of the designers of Moby Dick, provided much useful information about its operation. We would also like to mention Bill Espensen, Vito Manzella, and Al Minn. We also benefited greatly from discussions of theoretical matters with Carl Dover, Sid Kahana, Leonard Kisslinger, Al Rosenthal, and Frank Tabakin. We thank them also for their interest in this project. This work was supported by the U. S. DOE. This work was submitted in partial fulfillment of requirements for the Ph.D. at Carnegie-Mellon University by D. Marlow.

*Present address: Computer Engineering Center, Mellon Institute of Science, Pittsburgh, Pennsylvania, 15213.

†Present address: Physics Department, MIT, Cambridge, Massachusetts, 02139.

‡Present address: Physics Department, Kyoto Sangyo University, Kyoto 603, Japan.

§Present address: Texaco Research Labs, Houston, Texas.

[1]J. M. Eisenberg and D. S. Koltun, *Theory of Meson Interactions with Nuclei* (Wiley, New York, 1980).

[2]R. Landau, in *Proceedings of the Eight International Conference on High Energy Physics and Nuclear Structure* (North-Holland, Amsterdam, 1980), p. 289.

[3]R. A. Eisenstein, in Proceedings of the Workshop on Nuclear and Particle Physics at Energies up to 31 GeV, edited by D. Bauman, L. Kisslinger, and R. Silbar, Los Alamos Scientific Laboratory Report LA-8775-C, 1981 p. 189.

[4]C. B. Dover and G. E. Walker, Phys. Rev. C 19, 1393 (1979).

[5]A. S. Rosenthal and F. Tabakin, Phys. Rev. C 22, 711 (1980).

[6]S. R. Cotanch, Proceedings of the Kaon Factory Workshop, Vancouver, 1979 TRIUMF report, 1979; S. R. Cotanch and F. Tabakin, Phys. Rev. C 15, 1379 (1977).

[7]Y. Sakamoto, Y. Hatsuda, and M. Toyama, Lett. Nuovo Cimento 27, 140 (1980).

[8]Y. Abgrall and J. Labarsouque, 9th International Conference on High Energy Physics and Nuclear Structure, Versailles, France, 1981.

[9]M. J. Paez and R. H. Landau (unpublished).

[10]L. S. Kisslinger and W. L. Wang, Ann. Phys. (N.Y.) 99, 374, 1976.

[11]M. Hirata, J. H. Koch, F. Lenz, and E. J. Moniz, Ann. Phys. (N.Y.) 120, 205 (1979).

[12]K. Klingenbeck, M. Dillig, and M. Huber, Phys. Rev. Lett. 41, 387 (1978).

[13]E. Oset and W. Weise, Nucl. Phys. A329, 365 (1979).

[14]L. S. Kisslinger, Phys. Rev. C 22, 1202 (1980).

[15]L. S. Kisslinger, Proceedings of the 15th Annual Los Alamos User's Group Meeting, LAMPF User's Group Newsletter (Los Alamos) 13, 25 (1981).

[16]C. Bricman *et al.*, Phys. Lett. 75B, 1 (1978).

[17]M. Alston-Garnjost, R. Kenney, D. Pollard, R. Ross, R. Tripp, and H. Nicolson, Phys. Rev. D 17, 2226, (1978).

[18]G. P. Gopal, R. T. Ross, A. J. Van Horn, A. C. McPherson, E. F. Clayton, T. C. Bacon, and I. Butterworth, Nucl. Phys. B119, 362 (1977).

[19]B. R. Martin, Nucl. Phys. B94, 413 (1975).

[20]G. Giacomelli *et al.*, Nucl. Phys. B71, 138 (1974).

[21]C. W. de Jager, H. de Vries, and C. de Vries, At. Data Nucl. Data Tables 14, 479 (1974).
[22]R. A. Eisenstein and G. A. Miller, Comput. Phys. Commun. 8, 130 (1974).
[23]R. Landau, S. C. Phatak, and F. Tabakin, Ann. Phys. (N.Y.) 78, 299 (1973); R. A. Eisenstein and F. Tabakin, Comput. Phys. Commun. 12, 237, 1976; and (unpublished).
[24]R. Cester-Regge and M. May, Brookhaven Internal Report, 1977.
[25]K. L. Brown, D. C. Carey, Ch. Iselin, and F. Rothacker, CERN Report CERN 80-04, SPS Division, 1980.
[26]MINUIT, by F. James and M. Roos, CERN Computer Center Library.
[27]C. Gustaffson and E. Lambert, Ann. Phys. (N.Y.) 111, 304 (1978).
[28]R. A. Eisenstein and G. A. Miller, Comput. Phys. Commun. 11, 95 (1976).
[29]V. Gillet and N. Vinh Mau, Nucl. Phys. 54, 321 (1964).
[30]C. J. Adams *et al.*, Nucl. Phys. B66, 36 (1973); S. Focardi *et al.*, Phys. Lett. 24B, 314 (1967).
[31]D. V. Bugg, R. S. Gilmore, K. M. Knight, D. C. Salter, G. H. Stafford, E. J. N. Wilson, J. D. Davies, J. D. Dowell, P. M. Hattersley, R. J. Horner, A. W. O'Dell, A. A. Carter, R. J. Tapper, and K. F. Riley, Phys. Rev. 168, 1466 (1968).